PAPER

Self-assembly of TiO_2/ZIF-8 nanocomposites for varied photocatalytic CO_2 reduction with H_2O vapor induced by different synthetic methods†

Yan-Hong Zou,‡ Hai-Ning Wang, [ID] ‡ Xing Meng, [ID] * Hong-Xu Sun and Zi-Yan Zhou [ID] *

Photoreduction of carbon dioxide (CO_2) provides an effective perspective for solving the energy crisis and environmental problems. Herein, two types of composite photocatalysts (TiO_2/ZIF-8) based on ZIF-8 and TiO_2 have been designed and synthesized with the help of the grinding method and the solid-synthesis method. Both composite photocatalysts are employed for the photocatalytic reduction of CO_2. In composite photocatalysts prepared by the grinding method, ZIF-8 particles are distributed on the surface of TiO_2, and provide extra available spaces for storing CO_2, which is beneficial for improving their photoreduction performances. As a result, an enhanced CO formation rate of 21.74 μmol g^{-1} h^{-1} with a high selectivity of 99% is obtained for this family of composite photocatalysts *via* the solid–gas mode without photosensitizers and sacrificial agents. For comparison, the other family of composite photocatalysts synthesized *via* the solid-synthesis method possesses structures similar to ZIF-8, where TiO_2 is encapsulated inside the framework of ZIF-8. This structural feature obstructs the contact between the active sites of TiO_2 and CO_2, and leads to lower activities. The best CO formation rate of this family is only 10.67 μmol g^{-1} h^{-1} with 90% selectivity. Both the structural features of the two families of photocatalysts are described to explain their differences in photoreduction performances. The experimental finding reveals that different synthetic approaches indeed result in diversified structures and varied photocatalytic performances. This work affords a new scalable and efficient approach for the rational design of efficient photocatalysts in the area of artificial photosynthesis.

1. Introduction

Carbon dioxide (CO_2) is mainly produced by the continuous combustion of fossil fuels, and has become a kind of greenhouse gas, which plays an important role in global warming. The growing concerns about global warming induced by the increase of CO_2 concentrations have drawn increasing attention in the CO_2 capture and conversion. Naturally, various approaches have been developed to overcome this problem.[1–10] Among the reported technologies, the conversion of CO_2 into valuable chemical materials by means of efficient photocatalysts may be an effective strategy with the help of solar energy, which is likely to resolve global warming. So, the development of outstanding photocatalysts for the photocatalytic reduction of CO_2 has become an active field of research.

In the past few decades, various kinds of photocatalysts have been designed and synthesized, and contain molecular compounds, semiconductors, and others.[11–30] Common problems of these photocatalysts are listed below: a high recombination of electron–hole pairs, poor CO_2 adsorption ability, and others.

It is urgent to prepare new photocatalysts with improved separation of electron–hole pairs, and enhanced CO_2 adsorption ability. Metal–organic frameworks (MOFs), as a new class of porous crystalline materials, are constructed from numerous metal ions and various organic linkers.[31–35] This kind of porous materials possesses following advantages: structural tunability, ordered porous structures and large surface area. These excellent characteristics make MOFs widely explored in various fields, such as sensors, energy storage and catalysis[36–42] However, it is in early stages that MOFs are employed as photocatalysts for reducing CO_2. A limited number of MOFs, such as UiOs[43–45] and MILs has made an attempt in this field. For example, a light-harvesting MOF, MIL-125–NH_2 (Ti), serves as a photocatalyst and can convert CO_2 into HCOOH.[44] These covered examples reveal that the photocatalytic activity of the

School of Chemistry and Chemical Engineering, Shandong University of Technology, Zibo 255049, People's Republic of China. E-mail: mengxing837@foxmail.com

‡ Yan-Hong Zou and Hai-Ning Wang made equal contributions to this paper.

individual MOF is usually not very good. Recently, pioneering examples have demonstrated that the combination of semiconductors with MOFs may be a good choice to enhance the CO_2 photoreduction efficiency. The resulting composite photocatalysts possess the advantages of each component (*e.g.*, strong CO_2 adsorption capacity of MOFs and good photocatalytic ability of semiconductors).[46] For instance, Wang *et al.*[47] covered a composite photocatalyst Co–ZIF-9/CdS with an enhanced CO_2 photoreduction performance. Naturally, it is necessary to develop more composite photocatalysts based on MOFs and semiconductors with great performance. As far as we know, most of the photocatalysts based on MOFs and semiconductors have been prepared with the help of conventional solvothermal or hydrothermal or bulk solution or wet-chemistry methods,[48] which require a multi-step process, long reaction time and large amount of solvents. In order to overcome the above problem, it could be very interesting to explore a simple and scalable synthetic approach to prepare MOF/semiconductor composite photocatalysts with improved photocatalytic performances. Directed by this idea, a facile synthetic method (the grinding method) is selected to fabricate TiO_2/ZIF-8 composite photocatalysts within a few minutes. ZIF-8 is chosen because of its high surface area and good stability towards water, which can guarantee the simultaneous absorption of water and CO_2, critical for the process of photoreducing CO_2. Finally, a variety of composite photocatalysts based on ZIF-8 and TiO_2 have been synthesized through this simple and efficient manner.

Up to now, most of the photocatalysts have been employed for the photoreduction of CO_2 *via* a solid–liquid mode in the presence of sacrificial agents (*e.g.*, triethanolamine) as electron donors, which are toxic and high-cost. Recently, another reaction mode (solid–gas mode) was developed to overcome this problem because this reaction mode does not need photosensitizers and sacrificial agents. In this reaction mode, CO_2 and H_2O molecules directly surround the photocatalyst. Meanwhile, H_2O offers protons and acts as a sacrificial agent. For example, Xiong *et al.*[49] employed this mode to evaluate the activity of $Cu_3(BTC)_2@TiO_2$ in the photoreduction of CO_2, which can selectively convert CO_2 into CH_4. Based on the above considerations, herein, a series of composite photocatalysts based on ZIF-8 and TiO_2 have been synthesized with the help of the grinding method. In this method, ZIF-8 particles are located at the surface of the TiO_2 spheres, which avoids the accumulation of TiO_2 spheres, and are responsible for storing CO_2. The obtained composite photocatalysts are evaluated for their CO_2 photoreduction performance *via* solid–gas mode without photosensitizers and sacrificial agents. The results show that the well-integrated structures prefer to enhance the CO_2 photoreduction performance. As a result, an enhanced CO formation rate of 21.74 μmol g^{-1} h^{-1} with a great selectivity of 99% was obtained. In order to verify the influence of the synthesis method on the photocatalytic reduction of CO_2, another series of composite photocatalysts have been synthesized *via* the solid-synthesis method. This series of photocatalysts possess a similar structure compared to ZIF-8, where TiO_2 is encapsulated into the framework of ZIF-8. These

structures are different from those of the photocatalysts obtained *via* the grinding method, and this structural feature hinders their CO_2 photoreduction performances, leading to lower activities. In summary, the experimental results reveal that different synthetic approaches generate varied structures and photocatalytic performances, possibly due to their different structural characteristics. Furthermore, the possible mechanism of the CO_2 photocatalytic reduction is also proposed.

2. Experimental section

2.1 Materials and instruments

All used reagents and solvents are commercially available and directly used. The used reagents are listed below: 2-methyl imidazole (2-IM), titanium tetraisopropanolate (Ti(OiPr)$_4$), ethanol, 5% Nafion solution, zinc acetate dehydrate (Zn(oAc)$_2$), sodium sulphate and terephthalic acid (TA). All reagents were purchased from Shanghai Macklin Biochemical Co., Ltd.

Fourier transform infrared spectroscopy (FT-IR) spectra were recorded with a Thermo Nicolet 5700 using KBr pellets for the sample. X-ray powder diffraction patterns of the samples were recorded on a Bruker D8 Advance diffractometer with Cu Kα (λ = 1.5418 Å) radiation in the range of 5–70°. The morphology analysis of the synthesized samples was collected on a scanning electron microscope (SEM, Sirion 200) at an acceleration voltage of 10 kV. X-ray photoelectron spectroscopy (XPS) measurements were carried out on a scanning X-ray microprobe (K-Alpha, Thermo Scientific) with Al α radiation and the C 1s peak at 284.8 eV as the internal standard. The UV-Vis absorption spectrum was obtained on a UV-2550 spectrophotometer (Shimadzu, Japan). The CO_2 adsorption/desorption measurements were conducted under the ambient condition of 298 K (ASAP 2020). Nitrogen adsorption–desorption isotherms were measured at 298 K on an ASAP 2460 instrument. Transmission electron microscopy (TEM) on a JEM-200CX apparatus was performed at an accelerating voltage of 200 kV.

2.2 Synthesis and preparations

2.2.1 Synthesis of TiO$_2$. Titanium tetraisopropanolate (400 μL) was added to the mortar, and grinded for 30 min. Then, the obtained powder was transferred to a 25 mL Teflon-sealed autoclave and heated at 120 °C for 12 hours.

2.2.2 Synthesis of ZIF-8. 2-Methyl imidazole (0.071 g) and zinc acetate dehydrate (0.071 g) were added to the mortar, and evenly mixed. Then, the mixture was grinded for 30 min, and transferred to a 25 mL Teflon-sealed autoclave and heated at 120 °C for 12 hours.

2.2.3 Synthesis of TiO$_2$/ZIF-8-GX. 2-Methyl imidazole (0.071 g) and zinc acetate dehydrate (0.071 g) were added to the mortar, and evenly mixed. Then, ethanol (200 μL) and a certain amount of titanium tetraisopropanolate (200, 300, 400 μL) were put into this mortar, and grinded for 30 min. Finally, the obtained mixture was transferred to a 25 mL Teflon-sealed autoclave and heated at 120 °C for 12 hours. The resulting samples were defined as **TiO$_2$/ZIF-8-GX** (X = 1, 2, and 3, respectively,

corresponding to 200, 300 and 400 μL titanium tetraisopropanolate).

2.2.4   Synthesis of TiO$_2$/ZIF-8-SX. The synthetic process was modified according to the reported literature.[50] 2-Methyl imidazole (0.71 g) and zinc acetate dehydrate (0.71 g) were added to a 25 mL Teflon-sealed autoclave, and evenly mixed. Then, titanium tetraisopropanolate (2, 3, 4 mL) was added, and the obtained mixture was transferred to a 25 mL Teflon-sealed autoclave and heated at 180 °C for 24 hours. Finally, the resulting powders were hydrolysed in the presence of water with pH = 11. The obtained samples were defined as **TiO$_2$/ZIF-8-SX** (X = 1, 2, and 3 respectively, corresponding to 2, 3, and 4 mL titanium tetraisopropanolate).

2.3   General catalytic reduction

2.3.1   Photocatalytic CO$_2$ reduction. The photocatalyst (1 mg) was dispersed in 1 mL ethanol, and then coated on 1 cm × 3 cm ITO glass. The cover range is 1 cm × 3 cm. The prepared samples were placed in a self-made photocatalytic reactor, and 150 μL distilled water was added at the bottom as the reducing agent. CO$_2$ was introduced into the reactor to replace the air and ensured that the reactor was full of CO$_2$. A LED lamp was used as the light source. After irradiation for 2 hours, 0.5 mL and 1.0 mL gas were taken and placed in a gas chromatography (GC 1120) instrument to determine the content of CO and H$_2$.

2.3.2   CO$_2$ photoreduction analysis. The electrochemical analyzer (CHI 760E) was used for the photoelectrochemical test and Mott–Schottky test with the standard three-electrode system. A sodium sulfate solution (0.2 mol L^{-1}) served as the electrolyte. The sample (1 mg) and 5% Nafion solution were added to 2 mL ethanol and mixed for 1 h, and then evenly dropped on a 1 cm × 2 cm ITO conductive glass as the working electrode. The reference electrode was the Ag/AgCl electrode, and the counter electrode was the platinum electrode.

2.3.3   Detection of hydroxyl radicals (OH·). The experimental condition is similar to that of the CO$_2$ photoreduction. The difference exists in that **TiO$_2$/ZIF-8-G2** is uniformly mixed with terephthalic acid (TA) (mass ratio = 5 : 1). The photogenerated OH· would react with TA to generate 2-hydroxyterephthalic acid (TAOH), which could be used to detect the generated OH·. After irradiation, the obtained sample is used for fluorescence measurements.

3.   Results and discussion

3.1   Structure and morphology

One family of TiO$_2$/ZIF-8 composite photocatalysts has been prepared by the grinding method using an *in situ* synthetic process (experiment details in Experimental section), and is defined as **TiO$_2$/ZIF-8-GX** (X = 1, 2 and 3, corresponding to the different volumes of used Ti(OiPr)$_4$). For comparison, another family of TiO$_2$/ZIF-8 composite photocatalysts was also prepared using the same reaction substrates with the help of the solid-synthesis method, namely **ZIF-8/TiO$_2$-SX** (X = 1, 2 and 3, corresponding to the different volumes of used Ti(OiPr)$_4$). In order to confirm the successful formation of ZIF-8 and TiO$_2$, all

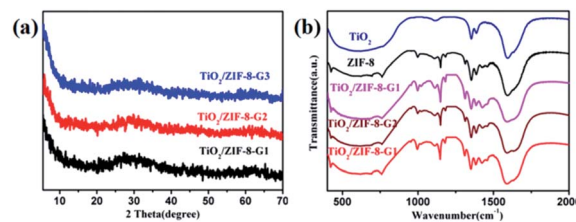**Fig. 1**   (a) PXRD patterns and (b) FT-IR spectra of TiO$_2$/ZIF-8-GX, ZIF-8 and TiO$_2$.

as-synthesized powders have been identified *via* the powder X-ray diffraction (PXRD) patterns. The crystallinities of **TiO$_2$/ZIF-8-GX** are not well-defined. Only several weak peaks (around 10.4°, 12.5° and 18.5°) are observed, which are consistent with the simulated PXRD pattern of ZIF-8 (Fig. 1a and S3†). In addition, there is a broad peak between 20° and 40° relative to TiO$_2$, which can be attributed to the anatase TiO$_2$ (JCPDS no. 21-1272).[51] Additionally, the PXRD patterns of **TiO$_2$/ZIF-8-SX** were performed. Their patterns exhibit good diffraction peaks, and match well with that of ZIF-8, implying that the good crystallinity of ZIF-8 is well maintained (Fig. S2†). It should be mentioned that a weak diffraction peak at 25.7° is responsible for the (101) plane of TiO$_2$.

In addition, the Fourier transform infrared (FT-IR) spectra were used to analyze the surface chemistry of the prepared TiO$_2$/ZIF-8 composite photocatalysts. As shown in Fig. 1b and S1,† the spectra of **TiO$_2$/ZIF-8-GX** and **TiO$_2$/ZIF-8-SX** composite photocatalysts constructed by different approaches are similar. In Fig. 1b, their characteristic peaks are clearly found in the FTIR spectra. The peaks around 996, 1423 and 1578 cm^{-1} are attributed to the C–N and C=N stretching vibrations from 2-IM,
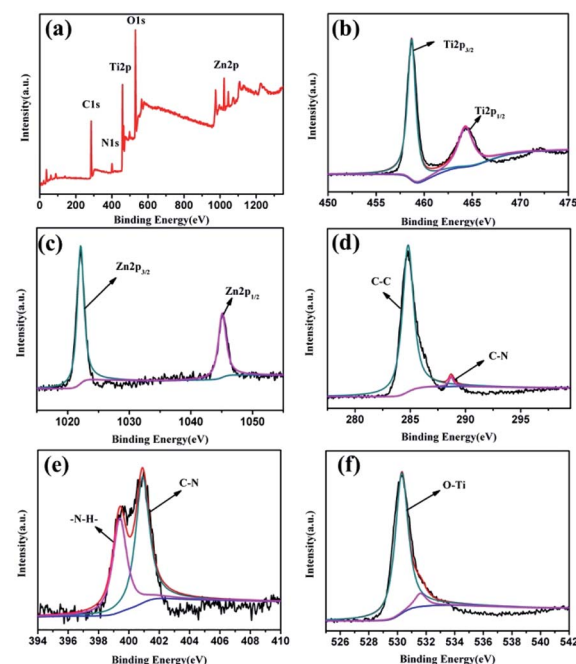

Fig. 2   (a) XPS survey of TiO$_2$/ZIF-8-G2, (b) Ti 2p, (c) Zn 2p, (d) C 1s, (e) N 1s and (f) O 1s spectra.

and the signals of the C–N bending vibration are demonstrated by the peaks located at around 1148 and 1308 cm^{-1}. Besides, the peak at 420 cm^{-1} in the spectra belongs to the stretching vibrations of the Zn–N bonds.[52,53] Additionally, the broad peaks from 500 to 800 cm^{-1} are ascribed to the stretching vibrations of the Ti–O bonds.[54,55] As shown in Fig. S1,† similar peaks are found in the spectra of **TiO$_2$/ZIF-8-SX**. The signals of the C–N and C=N stretching vibrations and the C–N bending vibrations are demonstrated by the peaks at around 998, 1421, 1582, 1145 and 1304 cm^{-1}. The peak located at 424 cm^{-1} corresponds to the Zn–N bonds. The broad peaks at around 500–790 cm^{-1} belong to the Ti–O bond stretching vibration.

X-ray photoelectron spectroscopy (XPS) has been used to study the chemical states and the composition of the prepared photocatalysts. The survey spectrum of **TiO$_2$/ZIF-8-G2** proves the presence of the Zn 2p, Ti 2p, N 1s, C 1s and O 1s peaks (Fig. 2a). The XPS spectrum of Ti exhibits two peaks at 458.6 eV and 464.3 eV, which are relative to the binding energies of Ti 2p$_{3/2}$ and Ti 2p$_{1/2}$, respectively (Fig. 2b). This implies the existence of the oxidation state Ti^{4+} in **TiO$_2$/ZIF-8-G2**. As seen in Fig. 2c, the binding energies at 1022.1 eV and 1045.1 eV belong to the Zn 2p$_{3/2}$ and Zn 2p$_{1/2}$, respectively. Fig. 2d shows that two peaks at around 284.7 eV and 288.5 eV are assigned to the C–C and C–N bonds from the imidazole groups in the C 1s spectrum, respectively. Additionally, in the spectrum of N, two peaks (399.3 and 400.9 eV) can be attributed to –NH– and C–N, respectively (Fig. 2e). In the O 1s spectrum, one main peak at 530.3 eV belongs to the Ti–O bonds, and the other peak with weak intensity at 531.6 eV is attributed to the lattice oxygen atoms in TiO$_2$ (Fig. 2f).[56,57] In summary, all characterization results indicate that the successful combination of TiO$_2$ and ZIF-8 has been realized.

The obtained photocatalysts have been used to evaluate their surface morphology with the help of scanning electron microscopy (SEM) images. The morphologies of ZIF-8, TiO$_2$ and **TiO$_2$/ZIF-8-GX** are found to be different by SEM images. The SEM images show that the particles of ZIF-8 possess the smooth surface and exhibit angular shapes (Fig. 3a and b). Fig. 3b shows that the as-synthesized TiO$_2$ particles are spherical with rough surfaces. In addition, the pure TiO$_2$ spheres can agglomerate
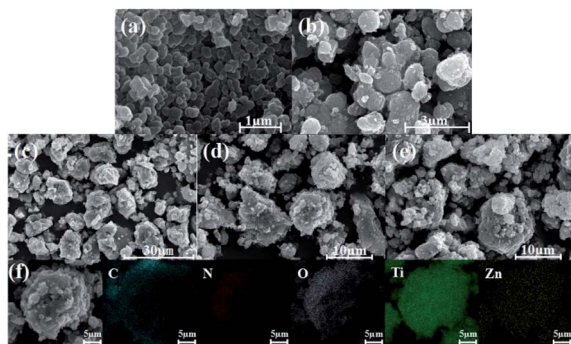

Fig. 3 SEM images of (a) ZIF-8, (b) TiO$_2$, (c) **TiO$_2$/ZIF-8-G1**, (d) **TiO$_2$/ZIF-8-G2**, (e) **TiO$_2$/ZIF-8-G3**, and (f) EDS elemental mapping images of **TiO$_2$/ZIF-8-G2**.
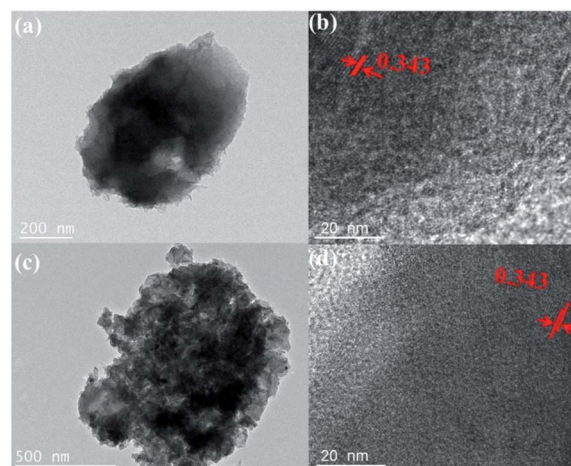

Fig. 4 TEM images of (a) **TiO$_2$/ZIF-8-G2**, (c) **TiO$_2$/ZIF-8-S2**, and high-resolution transmission electron microscope (HRTEM) images of (b) **TiO$_2$/ZIF-8-G2**, (d) **TiO$_2$/ZIF-8-G2**.

together. As shown in Fig. 3c–e, most of the particles also maintain the sphere shape, but possess rougher surfaces, compared with that of the pure TiO$_2$ spheres, indicating that the ZIF-8 particles have successfully coated the surfaces of the TiO$_2$ spheres. The coating of ZIF-8 make **TiO$_2$/ZIF-8-GX** greatly avoid the agglomeration of TiO$_2$, which may enhance their catalytic activity. The elemental distribution of **TiO$_2$/ZIF-8-GX** has been carried out with the help of element mapping. Fig. 3f clearly displays the element distribution of **TiO$_2$/ZIF-8-G2**, where the cyan, red, grey, green and yellow colours represent the distributions of each element C, N, O, Ti and Zn, respectively. With the help of the element mapping, we can confirm that ZIF-8 was successfully located on the surface of the TiO$_2$ spheres. Summarily, in **TiO$_2$/ZIF-8-GX**, ZIF-8 is located at the surface of the TiO$_2$ spheres. In order to justify our hypothesis, taking **TiO$_2$/ZIF-8-G2** as an example, transmission electron microscope (TEM) images have been used to prove this result. As shown in Fig. 4a and b, the generated TiO$_2$ nanoparticles are surrounded by ZIF-8, and the peripheral surface is terminated by ZIF-8. The generated TiO$_2$ presents a plane spacing with the value of approximately 0.343 nm (Fig. 4b), which is relative to the (101) lattice plane of the generated TiO$_2$. Meanwhile, the SEM images (Fig. S4†) show that the particles of **TiO$_2$/ZIF-8-SX** are held together and **TiO$_2$/ZIF-8-SX** exhibits similar morphology, compared to that of ZIF-8. Moreover, the TEM images (Fig. 4c and d) of **TiO$_2$/ZIF-8-S2** are provided, demonstrating the existence of TiO$_2$, and indicate that TiO$_2$ may be embedded into the framework of ZIF-8 together with its SEM image.[48] The photocatalysts prepared by different methods possess different structures. The above results show that the synthetic method employed for preparing the composite photocatalyst has an important influence on the structure and morphology of the samples.

3.2 Photocatalytic activity

The photoreduction of CO$_2$ has been carried out through a solid–gas reaction mode by placing TiO$_2$, ZIF-8 and TiO$_2$/ZIF-8

photocatalysts in a homemade reactor full of CO_2 and several drops of water. This reaction mode is chosen due to its relative high product selectivity, and inhibited comparative H_2 generation reaction. The detailed experimental results of various photocatalysts on the CO_2 photoreduction are present and given in Fig. 6. It is obvious that CO and trace H_2 have been observed for all samples. It should be mentioned that **TiO$_2$/ZIF-8-GX** creates a high selectivity for CO_2 photoreduction. The formation rate of CO increases from 14.63 to 21.74 μmol g^{-1} h^{-1}, and then decreases to 15.9 μmol g^{-1} h^{-1} after irradiation for 2 h. Conversely, the as-synthesized TiO_2 and ZIF-8 exhibited CO formation rates of 7.53 and 1.87 μmol g^{-1} h^{-1}, respectively, under the same experimental conditions, revealing their much lower CO_2 photoreduction efficiencies.

In order to investigate the influence of the synthetic method on the photocatalytic performances, the solid synthesis method was used to prepare this type of photocatalyst. Then, the composite photocatalysts prepared *via* the solid synthesis method were employed to evaluate their ability for reducing CO_2. These photocatalysts possess similar photocatalytic behaviours. Three samples have similar formation rates of CO after irradiation for 2 h (9.82, 10.67 and 9.80 μmol g^{-1} h^{-1} for **TiO$_2$/ZIF-8-S1**, **TiO$_2$/ZIF-8-S2** and **TiO$_2$/ZIF-8-S3**, respectively). Naturally, **TiO$_2$/ZIF-8-S2** exhibits the best performance. Obviously, the CO formation rates of **TiO$_2$/ZIF-8-SX** are lower than those of **TiO$_2$/ZIF-8-GX**. Summarily, **TiO$_2$/ZIF-8-SX** exhibited inferior activities compared to the performances of **TiO$_2$/ZIF-8-GX**. The different photocatalytic performances of two kinds of photocatalysts may probably result from their different structures. In order to excavate the influence of the structure on the photocatalytic performance, TiO_2 from the etching of **TiO$_2$/ZIF-8-G2** and **TiO$_2$/ZIF-8-S2** was collected and employed to evaluate their photocatalytic performances. It should be mentioned that the crystallinity of TiO_2 resulting from **TiO$_2$/ZIF-8-G2** is lower than that of TiO_2 obtained from **TiO$_2$/ZIF-8-S2**, confirmed by their PXRD patterns (Fig. S5†). The formation rates of CO are 7.50 and 5.88 μmol g^{-1} h^{-1}, respectively (Fig. S6†), and TiO_2 derived from **TiO$_2$/ZIF-8-G2** exhibited better photocatalytic

performances than that of TiO_2 from **TiO$_2$/ZIF-8-S2**. The experimental results reveal that TiO_2 with low crystallinity is beneficial for CO_2 reduction.[58] Exposed defects induced by the low crystallinity of TiO_2 in **TiO$_2$/ZIF-8-GX** can facilitate the separation of photogenerated electrons and holes, which favours the improvement of photocatalytic activities. ICP measurements have also been performed. The calculated results display that two types of photocatalysts possess different molar ratios of Ti to Zn, and the molar ratios of Ti to Zn in **TiO$_2$/ZIF-8-GX** are higher (Tables S1 and S2†), indicating that **TiO$_2$/ZIF-8-GX** could provide more reaction actives. Besides, the distribution of ZIF-8 at the surface of TiO_2 in **TiO$_2$/ZIF-8-GX** not only enriches CO_2, but also prevents the aggregation of TiO_2. In a word, the structural features of **TiO$_2$/ZIF-8-GX** prefer to reduce CO_2 under the irradiation of light. Conversely, the structures of **TiO$_2$/ZIF-8-SX** are unfavourable to reduce CO_2 because TiO_2 with good crystallinity cannot suppress the separation of photogenerated electrons and holes effectively, and the photocatalytic active sites of TiO_2 are difficult to form contacts with CO_2 because they are trapped in the skeleton of ZIF-8.

The experimental phenomena show that the introduction of ZIF-8 indeed improves the CO_2 photoreduction performances of the composite photocatalysts. The optimized performance comes from **TiO$_2$/ZIF-8-G2**, and its photocatalytic production yields at the given times are 5.04, 13.38, 31.85 and 43.49 μmol g^{-1} (Fig. 6c). Compared to the original TiO_2 and ZIF-8, as well as TiO_2 derived from **TiO$_2$/ZIF-8-G2** and **TiO$_2$/ZIF-8-S2**, the photocatalytic efficiency of **TiO$_2$/ZIF-8-G2** increases by two, eleven and two times, respectively. For composite photocatalysts with varied amounts of TiO_2, the experimental results reveal that the photocatalytic performances improve first, and then decrease along with the increased amount of TiO_2. We speculate that the increased mass ratio of TiO_2 could provide more reactive sites. However, too much TiO_2 hinders the CO_2 absorption ability of the composite photocatalysts, suppressing the benefits of the increased active sites. The enhanced photocatalytic performance of **TiO$_2$/ZIF-8-GX** is mainly due to the well-integrated
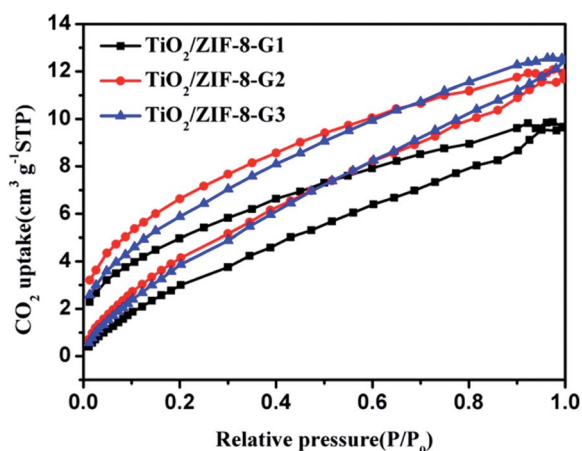

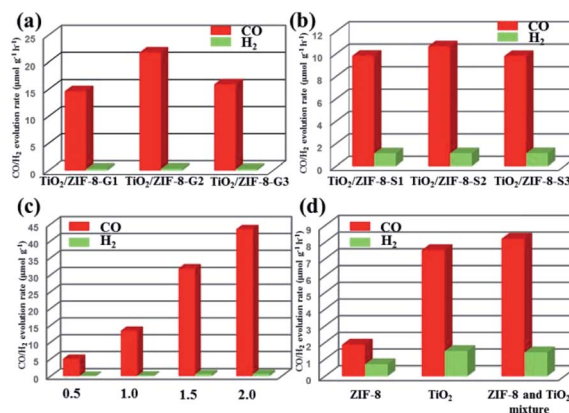**Fig. 5** CO_2 adsorption and desorption isotherm curves of **TiO$_2$/ZIF-8-GX**.

Fig. 6 (a) CO and H_2 yields of **TiO$_2$/ZIF-8-GX** and (b) **TiO$_2$/ZIF-8-SX**. (c) Time–yield plots of CO and H_2 over **TiO$_2$/ZIF-8-G2** composites under light illumination. (d) CO and H_2 yields of ZIF-8, TiO_2, and ZIF-8 and the TiO_2 mixture.

Table 1 Comparisons between $TiO_2/ZIF-8-G2$ and other photocatalysts based on MOFs and semiconductors

Photocatalyst	Product and its formation rate ($\mu mol\ g^{-1}\ h^{-1}$)	Reaction agent	Light source	Ref.
TiO_2–Co–ZIF-9	CO 8.80, CH_4 2.00, H_2 2.60	H_2O vapor, 50 mg catalyst	300 W Xe lamp	61
TiO_2–Mg–CPO-27	CO 4.09, CH_4 2.35	H_2O vapor, 10 mg catalyst	4 W LED lamp	62
$CsPbBr_3$ QDs/UiO-66(NH_2)	CO 8.21	10 mg	300 W Xe lamp	63
G-CNQDs/PMOF	CO 16.10, CH_4 6.86	MeCN/TEOA (4 : 1)	300 W Xe lamp	64
CNNS–UiO66(Zr)	CO 9.90	MeCN/TEOA (4 : 1)	300 W Xe lamp	65
$CsPbBr_3$@ZIF-67	CH_4 29.63	Films (mass of about 4.5 mg)	100 W Xe lamp	66
$Cu_3(BTC)_2$@TiO_2	CH_4 2.64	CO_2/H_2O vapor	300 W xenon arc lamp	67
$TiO_2/ZIF-8-G2$	CO 21.74	H_2O vapor, 1 mg catalyst	40 W LED lamp	This work

structure, and could result from the following issues: (i) ZIF-8 in the composites owns a large surface area, and is favourable for capturing CO_2; (ii) the distribution of ZIF-8 in the TiO_2 matrix can effectively avoid the aggregation of TiO_2 and make TiO_2 expose more reaction active sites; (iii) the low crystallinity of **$TiO_2/ZIF-8-GX$** can create more defects at the surface, which can accelerate the separation of the photogenerated electrons and holes. Naturally, the above factors make **$TiO_2/ZIF-8-GX$** possess high photocatalytic activity.

Previous achievements have demonstrated that the great CO_2 adsorption capability can benefit from enhancing the photocatalytic performance.[59–62] Naturally, the CO_2 absorption capacities of all samples have been evaluated at room temperature. The experimental findings exhibit **$TiO_2/ZIF-8-GX$** with CO_2 uptakes of 9.9, 12.1 and 12.6 $cm^3\ g^{-1}$ (Fig. 5) at 298 K, respectively. **$TiO_2/ZIF-8-SX$** exhibited CO_2 uptakes of 9.84, 9.87 and 11.59 $cm^3\ g^{-1}$ (Fig. S7†) at 298 K, which are lower than those of the corresponding **$TiO_2/ZIF-8-GX$**. ZIF-8 shows a CO_2 uptake of 17.0 $cm^3\ g^{-1}$,[63] while TiO_2 exhibits nearly no adsorption of CO_2.

To demonstrate that the product actually comes from the photoreduction of CO_2, the control experiments were performed. First, the homemade reactor in the absence of photocatalysts does not respond to light irradiation. Second, **$TiO_2/ZIF-8-G2$** shows no photocatalytic responses in N_2 and H_2O vapours. When CO_2 is used to replace N_2, a remarkable photocatalytic response is observed. Similar experimental findings can also be achieved for TiO_2 and **$TiO_2/ZIF-8-S2$**. In addition, the control experiment employing a physical mixture of TiO_2 and ZIF-8 as photocatalysts exhibits lower activity than those of **$TiO_2/ZIF-8-GX$**, and its formation rate of CO is 8.21 $\mu mol\ g^{-1}\ h^{-1}$.

In order to highlight the excellence of our work, the previous covered photocatalysts based on MOF and semiconductors are summarized and listed in Table 1. Naturally, the reported experimental findings are used for comparison with precious experimental results.[64–70] As shown in Table 1, most of the photocatalysts can only convert CO_2 into CO, and the photocatalytic performance of **$TiO_2/ZIF-8-G2$** is located at a high level compared to other similar photocatalysts. This comparison implies that the structure of **$TiO_2/ZIF-8-GX$** is favourable for the photocatalytic reduction of CO_2.

3.3 Optical and electrochemical properties

The UV-Vis diffuse reflectance spectra of ZIF-8, TiO_2 and **$TiO_2/ZIF-8-GX$**, as well as **$TiO_2/ZIF-8-SX$** have been measured to evaluate their light absorption ability (Fig. 7a and S9†). The prepared TiO_2 shows a steep absorption edge situated at about 350 nm. ZIF-8 can only adsorb UV light from 200 nm to 250 nm (Fig. S8†). **$TiO_2/ZIF-8-G1$** and **$TiO_2/ZIF-8-G3$** also show steep absorption edges around 350 nm, similar to that of TiO_2. Additionally, for **$TiO_2/ZIF-8-SX$**, their adsorption edges are located at about 350 nm, having similar light absorption ability. The spectra clearly reveal that **$TiO_2/ZIF-8-G2$** has a wider absorption band, compared to other photocatalysts, which indicates that it possesses a stronger light absorption capacity. **$TiO_2/ZIF-8-G2$** exhibits an expanded absorption edge at about 400 nm. The band gaps of TiO_2, ZIF-8 and **$TiO_2/ZIF-8-G1/2/3$** are
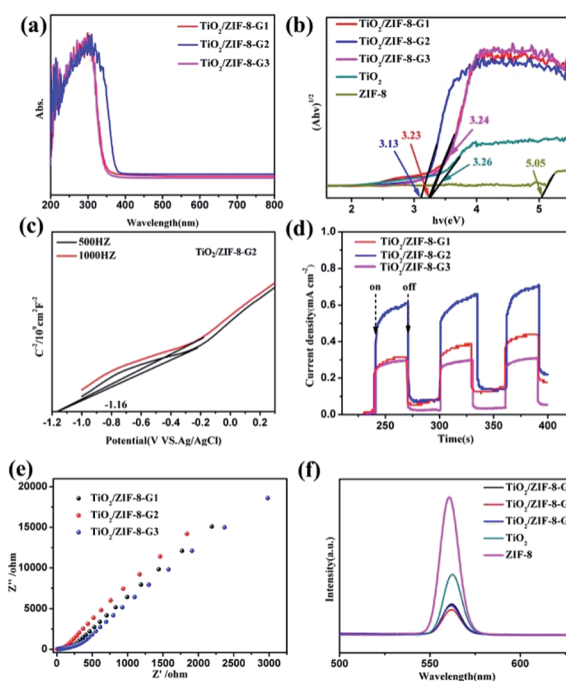

Fig. 7 (a) UV-Vis diffuse reflectance spectra of **$TiO_2/ZIF-8-GX$**. (b) Tauc plots of **$TiO_2/ZIF-8-GX$**, TiO_2 and ZIF-8. (c) Mott–Schottky plots of **$TiO_2/ZIF-8-G2$**. (d) Photocurrents of **$TiO_2/ZIF-8-GX$**. (e) Nyquist plots of **$TiO_2/ZIF-8-GX$**. (f) Photoluminescence spectra of **$TiO_2/ZIF-8-GX$**, TiO_2 and ZIF-8 (λ_{ex} = 325 nm).

calculated to be 3.26 eV, 5.05 eV, 3.23 eV, 3.13 eV, 3.24 eV by the Kubelka–Munk (KM) method, respectively (Fig. 7b). With the help of the same calculation method, the band gaps of **TiO$_2$/ZIF-8-S1/2/3** are obtained to be 3.26 eV, 3.25 eV and 3.27 eV, respectively. To reveal their band structures, the Mott–Schottky (MS) measurements of TiO$_2$, ZIF-8 and **TiO$_2$/ZIF-8-G1/2/3**, as well as **TiO$_2$/ZIF-8-S1/2/3**, were also carried out (Fig. 7c, S10 and S11†). With the help of the Mott–Schottky equations, the electronic band positions of **TiO$_2$/ZIF-8-GX** and **TiO$_2$/ZIF-8-SX** could be found. The conduction band (CB) positions of **TiO$_2$/ZIF-8-G1/2/3** and **TiO$_2$/ZIF-8-S1/2/3** were determined to be −1.08, −1.14, −1.10, −1.02, −1.07 and −1.06 eV (*vs.* Ag/AgCl), respectively. Their valence band (VB) positions were calculated to be 2.13, 1.97, 2.12, 2.24, 2.23 and 2.21 eV, respectively, according to the band gaps coming from the UV-Vis absorption data (Fig. 7b). Naturally, the energy band structures of TiO$_2$ and ZIF-8 can be established based on this calculation, and is shown in Fig. S10.† Among all photocatalysts, it is clearly shown that the CB position of **TiO$_2$/ZIF-8-G2** is more negative than the reduction potential of CO$_2$ converting into CO, which makes it easier to photoreduce CO$_2$.

The photocurrent density spectra are able to reflect the separation ability of the photo-induced charges. These data of all composite photocatalysts clearly reveal that the photocurrent density increases in the order of **TiO$_2$/ZIF-8-S3** < **TiO$_2$/ZIF-8-S1** < **TiO$_2$/ZIF-8-S2** < **TiO$_2$/ZIF-8-G3** < **TiO$_2$/ZIF-8-G1** < **TiO$_2$/ZIF-8-G2** (Fig. 7d and S9c†). Obviously, the photocurrent responses of **TiO$_2$/ZIF-8-GX** are stronger than those of **TiO$_2$/ZIF-8-SX**, which are consistent with their photocatalytic results. Among them, **TiO$_2$/ZIF-8-G2** possesses the maximum photocurrent density under the irradiation of light, and its high photocurrent response can be ascribed to the lower recombination rate of photogenerated electrons and holes pairs. Besides, the electrochemical impedance spectrum (EIS) is demonstrated to be a promising method for investigating the interfacial charge transfer. As shown in Fig. 7e and S9d,† the EIS plots of **TiO$_2$/ZIF-8-G2** show the smallest radius among all **TiO$_2$/ZIF-8-GX** photocatalysts. Smaller resistances result in better conductivity and prefer to transfer the photogenerated electrons. It should be mentioned that the smallest radius of **TiO$_2$/ZIF-8-G2**

corresponds to the result of the photocurrent measurements and CO$_2$ photoreduction performance.

In addition, the photoluminescence (PL) emission spectra of **TiO$_2$/ZIF-8-GX**, ZIF-8 and TiO$_2$ were performed to study the ability of the photogenerated charge carrier transfer. As shown in Fig. 7f, the PL emissions of **TiO$_2$/ZIF-8-GX** were quenched significantly compared to those of ZIF-8 and TiO$_2$, revealing the inhibited photoinduced charge recombination existing in **TiO$_2$/ZIF-8-GX**. This is because the defects induced by the low crystallinity of **TiO$_2$/ZIF-8-GX** offer many charge transfer pathways for photogenerated electrons. Additionally, the ZIF-8 shell makes an important contribution to the transfer of photogenerated electrons due to its more positive conduction band. Both of them hinder the recombination of photoelectrons and holes, resulting in enhanced photocatalytic performances.

4.   Possible photocatalytic mechanism

The possible CO$_2$ photoreduction reaction pathways of **TiO$_2$/ZIF-8-GX** and the corresponding possible mechanism are proposed to explain the synergistic effects between TiO$_2$ and ZIF-8 on the photocatalytic reduction of CO$_2$ (Fig. 8). This is because ZIF-8 possesses a large surface area, and is mainly responsible for CO$_2$ and H$_2$O uptake. CO$_2$ and water molecules first enter the pores of ZIF-8, and can subsequently migrate to the surface of TiO$_2$ through interconnected channels in the framework. Under the irradiation of light, several common intermediates (*e.g.*, CO$_3^{2-}$)[49] are generated with the help of the chemisorption between CO$_2$ and the surface of TiO$_2$. TiO$_2$ serves as the photocatalyst, and produces electrons and holes. Naturally, the photogenerated electrons gather together at the interfaces between TiO$_2$ and ZIF-8, and then take part in the photoreduction of abundant CO$_2$ and H$_2$O inside ZIF-8, promoting the progress of the photocatalytic reaction (Fig. 8). Meanwhile, the adsorbed water forms contacts with the holes in TiO$_2$, and then produces protons and OH˙.[71] The appearance of this process is demonstrated by the successful detection of OH˙ (Fig. S12†). Finally, the intermediates produce the final product of CO with the help of the generated electrons and protons.

5.   Conclusions

In summary, various binary semiconductor/ZIF photocatalysts (TiO$_2$/ZIF-8) have been fabricated with the help of the grinding method and the solid synthesis method. The photocatalysts prepared by the grinding method exhibit better photocatalytic performances than those of the photocatalysts fabricated by the solid synthesis method. The experimental finding demonstrates that different synthetic methods result in varied photocatalytic performances, caused by their different structural features. The resulting **TiO$_2$/ZIF-8-GX** exhibits enhanced photocatalytic reduction efficiencies toward CO$_2$ compared to pure TiO$_2$ and ZIF-8, as well as **TiO$_2$/ZIF-8-SX**, and **TiO$_2$/ZIF-8-G2** exhibits the highest CO formation rate of 21.74 μmol g^{-1} h^{-1}. The good performance could be attributed to the enhanced CO$_2$
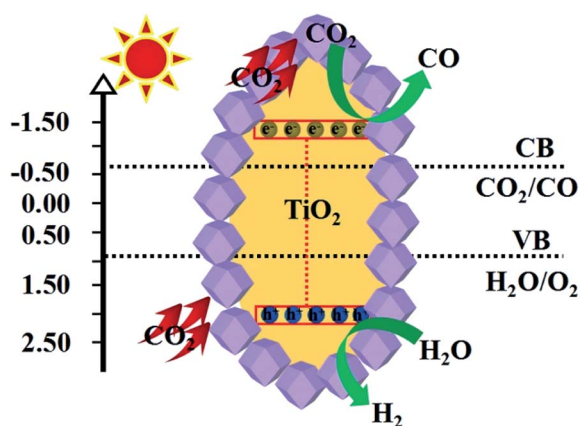

Fig. 8   Possible mechanism of TiO$_2$/ZIF-8-G2 for photoreducing CO$_2$.

absorption ability and the well-integrated structure, which can expose more active sites and absorb more CO_2. This work may offer some guidance for designing composited photocatalysts with high efficiency.

Conflicts of interest

There are no conflicts to declare.

Acknowledgements

References

1 Z. Sun, N. Talreja, H. Tao, J. Texter, M. Muhler, J. Strunk and J. Chen, *Angew. Chem., Int. Ed.*, 2018, **57**, 760.

2 J. L. White, M. F. Baruch, J. E. Pander, Y. Hu, I. C. Fortmeyer, J. E. Park, T. Zhang, K. Liao, J. Gu, Y. Yan, T. W. Shaw, E. Abelev and A. B. Bocarsly, *Chem. Rev.*, 2015, **115**, 12888.

3 L. J. Wang, R. l. Wang, X. Zhang, J. l. Mu, Z. Y. Zhou and Z. M. Su, *ChemSusChem*, 2020, **13**, 2973.

4 H. Huang, J. Lin, G. Zhu, Y. Weng, X. Wang, X. Fu and J. Long, *Angew. Chem., Int. Ed.*, 2016, **55**, 8314.

5 W. Kim, E. Edri and H. Frei, *Acc. Chem. Res.*, 2016, **49**, 1634.

6 X. Liu, S. Inagaki and J. Gong, *Angew. Chem., Int. Ed.*, 2016, **55**, 14924.

7 X. Liu, J. Iocozzia, Y. Wang, X. Cui, Y. Chen, S. Zhao, Z. Li and Z. Lin, *Energy Environ. Sci.*, 2017, **10**, 402.

8 M. Lu, J. Liu, Q. Li, M. Zhang, M. Liu, J. L. Wang, D. Q. Yuan and Y. Q. Lan, *Angew. Chem., Int. Ed.*, 2019, **58**, 12392.

9 M. Lu, Q. Li, J. Liu, F. M. Zhang, L. Zhang, J. L. Wang, Z. H. Kang and Y. Q. Lan, *Appl. Catal., B*, 2019, **254**, 624.

10 H. Zhang, J. Wei, J. Dong, G. Liu, L. Shi, P. An, G. Zhao, J. Kong, X. Wang, X. Meng, J. Zhang and J. Ye, *Angew. Chem., Int. Ed.*, 2016, **55**, 14310.

11 M. Zhang, M. Lu, Z. L. Lang, J. Liu, M. Liu, J. N. Chang, L. Y. Li, L. J. Shang, M. Wang, S. L. Li and Y.-Q. Lan, *Angew. Chem., Int. Ed.*, 2020, **59**, 2.

12 Y. H. Luo, L. Z. Dong, J. Liu, S. L. Li, Y. Q. Lan, W. G. Tu, Y. Zhou and Z. G. Zou, *Coord. Chem. Rev.*, 2019, **390**, 86.

13 K. Li, B. Peng and T. Peng, *ACS Catal.*, 2016, **6**, 7485.

14 C. l. Wang, Z. X. Sun, Y. Zheng and Y. H. Hu, *J. Mater. Chem. A*, 2019, **7**, 865.

15 L. F. Wei, C. L. Yu, Q. H. Zhang, H. Liu and Y. Wang, *J. Mater. Chem. A*, 2018, **6**, 22411.

16 M. Marszewski, S. W. Cao, J. G. Yu and M. Jaroniec, *Mater. Horiz.*, 2015, **2**, 261.

17 G. Sneddon, A. Greenaway and H. H. P. Yiu, *Adv. Energy Mater.*, 2014, **4**, 1301873.

18 M. Lu, Q. Li, J. Liu, F. M. Zhang, L. Zhang, J. L. Wang, Z. H. Kang and Y. Q. Lan, *Appl. Catal., B*, 2019, **254**, 624.

19 Y. Ma, X. Wang, Y. Jia, X. Chen and H. L. Han, *Chem. Rev.*, 2014, **114**, 9987.

20 D. Chen, X. G. Zhang and A. F. J. Lee, *J. Mater. Chem. A*, 2015, **3**, 14487.

21 S. W. Cao, J. X. Low, J. G. Yu and M. Jaroniec, *Adv. Mater.*, 2015, **27**, 2150.

22 S. N. Habisreutinger, L. Schmidt-Mende and J. K. Stolarczyk, *Angew. Chem., Int. Ed.*, 2013, **52**, 7372.

23 Y. P. Yuan, L. W. Ruan, J. Barber, S. C. J. Loo and C. Xue, *Energy Environ. Sci.*, 2014, 7, 3934.

24 N. Linares, A. M. Silvestre-Albero, E. Serrano, J. Silvestre-Albero and J. García-Martínez, *Chem. Soc. Rev.*, 2014, **43**, 7681.

25 H. Q. Sun and S. B. Wang, *Energy Fuels*, 2014, **28**, 22.

26 Q. J. Xiang, B. Cheng and J. G. Yu, *Angew. Chem., Int. Ed.*, 2015, **54**, 11350.

27 T. Zhang and W. B. Lin, *Chem. Soc. Rev.*, 2014, **43**, 5982.

28 S. Kumar, M. Y. Wani, C. T. Arranja, J. A. Silva, B. Avula and A. J. Sobral, *J. Mater. Chem. A*, 2015, **3**, 19615.

29 J. Y. Wang, B. S. Liu and K. Nakata, *Chin. J. Catal.*, 2019, **40**, 403.

30 C. Z. Wen, Q. H. Hu, Y. N. Guo, X. Q. Gong, S. Z. Qiao and H. G. Yang, *Chem. Commun.*, 2011, **47**, 6138.

31 P. Zhou, J. G. Yu and M. Jaroniec, *Adv. Mater.*, 2014, **26**, 4920.

32 M. Yaghi, H. L. Li, C. Davis, D. Richardson and T. L. Groy, *Acc. Chem. Res.*, 1998, **31**, 474.

33 B. Moulton and M. J. Zaworotko, *Chem. Rev.*, 2001, **101**, 1629.

34 X. Meng, H. N. Wang, S. Y. Song and H. J. Zhang, *Chem. Soc. Rev.*, 2017, **46**, 464.

35 H. N. Wang, X. Meng, L. Z. Dong, Y. Chen, S. L. Li and Y. Q. Lan, *J. Mater. Chem. A*, 2019, **7**, 24059.

36 X. Meng, Y. H. Zou, Y. Y. Zhang and L. S. Wang, *Journal of Liaocheng University*, 2019, **32**, 90.

37 S. M. J. Rogge, A. Bavykina, J. Hajek, H. Garcia, A. I. Olivos-Suarez, A. Sepúlveda-Escribano, A. Vimont, G. Clet, P. Bazin, F. Kapteijn, M. Daturi, E. V. Ramos-Fernandez, F. X. L. Xamena, V. V. Speybroeck and J. Gascon, *Chem. Soc. Rev.*, 2017, **46**, 3134.

38 W. P. Lustig, W. S. Mukherjee, N. D. Rudd, A. V. Desai, J. Li and S. K. Ghosh, *Chem. Soc. Rev.*, 2017, **46**, 3242.

39 K. Fujie and H. Kitagawa, *Coord. Chem. Rev.*, 2016, **370**, 382.

40 X. Meng, H. N. Wang, X. K. Wang, L. Z. Dong and Y. H. Zou, *New J. Chem.*, 2019, **43**, 24.

41 X. Meng, H. N. Wang, Y. H. Zou, L. S. Wang and Z. Y. Zhou, *Dalton Trans.*, 2019, **48**, 10422.

42 H. N. Wang, M. Zhang, A. M. Zhang, F. C Shen, X. K. Wang, S. N. Sun, Y. J. Chen and Y. Q. Lan, *ACS Appl. Mater. Interfaces*, 2018, **10**, 32265.

43 X. Meng, H. N. Wang, L. S. Wang, Y. H. Zou and Z. Y. Zhou, *CrystEngComm*, 2019, **21**, 3146.

44 C. Wang, Z. G. Xie, K. E. deKrafft and W. L. Lin, *J. Am. Chem. Soc.*, 2011, **133**, 13445.

45 Y. H. Fu, D. R. Sun, Y. J. Chen, R. K. Huang, Z. X. Ding, X. Z. Fu and Z. H. Li, *Angew. Chem., Int. Ed.*, 2012, **51**, 3364.

46 H. Q. Xu, J. H. Hu, D. K. Wang, Z. H. Li, Q. Zhang, Y. Luo, S. H. Yu and H. L. Jiang, *J. Am. Chem. Soc.*, 2015, **137**, 13440.

47 Q. Liu, Z. X. Low, L. X. Li, A. Razmjou, K. Wang, J. F. Yao and H. T. Wang, *J. Mater. Chem. A*, 2013, **1**, 11563.

48 S. B. Wang and X. C. Wang, *Appl. Catal., B*, 2015, **162**, 494.

49 X. He, Z. R. Gan, S. Fisenko, D. W. Wang, H. M. El-Kaderi and W. N. Wang, *ACS Appl. Mater. Interfaces*, 2017, **9**, 9688.

50 L. Z. Zhai, Y. H. Qian, Y. X. Wang, Y. D. Cheng, J. Q. Dong, S. B. Peh and D. Zhao, *ACS Appl. Mater. Interfaces*, 2018, **10**, 36933.

51 R. Li, J. H. Hu, M. S. Deng, H. L. Wang, X. J. Wang, Y. L. Hu, H. L. Jiang, J. Jiang, Q. Zhang, Y. Xie and Y. J. Xiong, *Adv. Mater.*, 2014, **26**, 4783.

52 W. L. Zhong, C. Li, X. M. Liu, X. K. Bai, G. S. Zhang and C. X. Lei, *Microporous Mesoporous Mater.*, 2020, **306**, 110401.

53 X. Zeng, L. Q. Huang, C. N. Wang, J. S. Wang, J. T. Li and X. T. Luo, *ACS Appl. Mater. Interfaces*, 2016, **8**, 20274.

54 Y. J. Ma, Q. Tang, W. Y. Sun, Z. Y. Yao, W. H. Zhu, T. Li and J. Y. Wang, *Appl. Catal., B*, 2020, **270**, 118856.

55 M. Zhang, Q. G. Shang, Y. Q. Wan, Q. R. Cheng, G. Y. Liao and Z. Q. Pan, *Appl. Catal., B*, 2019, **241**, 149.

56 Y. Zhang, W. Q. Cui, W. J. An, L. Liu, Y. H. Liang and Y. F. Zhu, *Appl. Catal., B*, 2018, **221**, 36.

57 R. Li, W. Li, C. Jin, Q. Y. He and Y. Z. Wang, *J. Alloys Compd.*, 2020, **825**, 154008.

58 Q. Chen, S. J. Wu, S. X. Zhong, B. J. Gao, W. J. Wang, W. H. Mo, H. J. Lin, X. X. Wei, S. Bai and J. R. Chen, *J. Mater. Chem. A*, 2020, **8**, 21208.

59 S. Wang, M. Xu, T. Peng, C. Zhang, T. Li, I. Hussain, J. Wang and B. Tan, *Nat. Commun.*, 2019, **10**, 676.

60 D. Wang, R. Huang, W. Liu, D. Sun and Z. Li, *ACS Catal.*, 2014, **4**, 4254.

61 R. Li, W. Zhang and K. Zhou, *Adv. Mater.*, 2018, **30**, 1705512.

62 M. Lu, Q. Li, J. Liu, F. M. Zhang, L. Zhang, J. L. Wang, Z. H. Kang and Y. Q. Lan, *Appl. Catal., B*, 2019, **254**, 624.

63 Y. Liu, L. Deng, J. P. Sheng, F. Y. Tang, K. Zeng, L. Q. Wang, K. X. Liang, H. Hu and Y. N. Liu, *Appl. Surf. Sci.*, 2019, **498**, 143899.

64 J. Wang, C. Xue, W. Q. Yao, J. Liu, X. X. Gao, R. L. Zong, Z. Yang, W. J. Jin and D. P. Tao, *Appl. Catal., B*, 2019, **250**, 369.

65 S. Yan, S. Q. Yang, H. Xu, M. Zhao, X. Zhang and J. Ye, *J. Mater. Chem. A*, 2016, **4**, 15126.

66 S. Wan, M. Ou, Q. Zhong and X. Wang, *Chem. Eng. J.*, 2019, **358**, 1287.

67 C. Zheng, X. Y. Qiu, J. Y. Han, Y. F. Wu and S. Q. Liu, *ACS Appl. Mater. Interfaces*, 2019, **11**, 42243.

68 N. Sadeghi, S. Sharifnia and M. Sheikh Arabi, *J. CO2 Util.*, 2016, **16**, 450.

69 Z. C. Kong, J. F. Liao, Y. J. Dong, Y. F. Xu, H. Y. Chen, D. B. Kuang and C. Y. Su, *ACS Energy Lett.*, 2018, **3**, 2656.

70 R. Li, J. Hu, M. Deng, H. Wang, X. Wang, Y. Hu, H. L. Jiang, J. Jiang, Q. Zhang, Y. Xie and Y. Xiong, *Adv. Mater.*, 2014, **26**, 4783.

71 H. N. Wang, H. Chen, L. L. Chen, W. H. Zhang, Z. Y. Zhou and X. Meng, *Res. Chem. Intermed.*, 2018, **44**, 1261.